Bindi, D., Spallarossa, D., Pacor, F. (2017): Between-event and between-station variability observed in the Fourier and response spectra domains: comparison with seismological models. - *Geophysical Journal International*, *210*, 2, pp. 1092—1104.

DOI: http://doi.org/10.1093/gji/ggx217

Geophysical Journal International

*Geophys. J. Int.* (2017) **210,** 1092–1104
Advance Access publication 2017 May 18
GJI Seismology

doi: 10.1093/gji/ggx217

# Between-event and between-station variability observed in the Fourier and response spectra domains: comparison with seismological models

D. Bindi,[1] D. Spallarossa[2] and F. Pacor[3]

[1] *Deutsches GeoForschungsZentrum GFZ, Potsdam, Germany. E-mail: bindi@gfz-potsdam.de*
[2] *Dipartimento di Scienze della Terra dell'Ambiente e della Vita, Universitá di Genova, Genoa, Italy*
[3] *Istituto Nazionale di Geofisica e Vulcanologia, Milan, Italy*

Accepted 2017 May 17. Received 2017 May 15; in original form 2016 December 7

## SUMMARY

In this study, we analyse a regional data set composed by about 9000 waveforms from 231 earthquakes in the magnitude range from 3 to 6 and recorded in central Italy in the time period 2008–2013. We derive a seismological model whose source, attenuation and site parameters are used to explain the ground motion variability associated with a set of ground motion prediction equation (GMPE) calibrated *ad hoc* for both Fourier and acceleration response spectra. The main results are the following: (1) the between-event residuals $\delta B_e$ show a clear dependence on the stress drop for frequencies above 2 Hz; (2) the standard deviation $\tau$ of $\delta B_e$ is strongly reduced (up to 80 per cent) by introducing in the functional form the stress drop values estimated from each source spectrum; (3) the standard deviation $\tau$ depends on the magnitude scale used to calibrate the GMPE: while the moment magnitude better describes the source variability at low frequency, the local magnitude better capture the source-related ground motion variability at frequencies larger than 2 Hz; (4) for frequencies higher than 10 Hz, the observed increase of $\tau$ with frequency correlate well with the attenuation parameter $k_{source}$, computed from the high-frequency slope of the source spectra. Regarding the station-to-station residuals $\delta$S2S, their frequency dependency is in good agreement with the site amplifications extracted from the *S*-wave spectra. Finally, while the overall dependences of the ground motion variability on seismological parameters are similar when observed either in the Fourier or in the response spectra domains (e.g. the dependency of the between event on stress drop), differences in the results suggest that the response spectra do not allow to fully capture the ground motion variability, as well as the site amplifications, at high frequencies.

**Key words:** Earthquake ground motions; Earthquake source observations; Seismic attenuation; Site effects.

## 1 INTRODUCTION

The prediction of the shaking generated by an earthquake at a given locality, and its spatial variability, are fundamental targets for any seismic hazard assessment. A wide spectrum of approaches to predict ground motion is available in the literature, ranging from empirical equations to simulation modelling (Douglas & Aochi 2008). Empirical ground motion prediction equations (GMPEs) are widely adopted in moderate-to-strong seismicity regions, while numerical simulations are generally performed in areas where strong-motion data sets are poor. Among simulation methods, the stochastic ones (Boore 2003; Motazedian & Atkinson 2005) are the most popular, reproducing the ground motion on the entire frequency-band over a wide range of magnitude and distance. The key element of the stochastic methods is the seismological model describing the source scaling, the attenuation with distance and the site amplifications. The parameters defining the seismological models can be empirically estimated, usually applying inversion or deconvolution methods to regional data sets (e.g. Drouet *et al.* 2008; Allmann & Shearer 2009; Baltay *et al.* 2011; Goertz-Allmann & Edwards 2014; Oth & Kaiser 2014).

Hybrid methods, in which empirical and seismological approaches are combined, have been proposed with the aim of extending the range of applicability of empirical models. Typically, these methods are developed for adjusting GMPEs from one region (the Host, rich of strong-motion recordings) to use in another region (the Target, lacking of data or located in a different tectonic environment). Examples are the hybrid empirical approach (Campbell 2003), the hybrid referenced empirical approach (Atkinson 2008) and their recent developments (e.g. Yenier & Atkinson 2015a) where

seismological models are used to develop the regional adjustments for the GMPE median values.

Well-calibrated seismological models (functional forms and parameters) can be also exploited to explain the ground motion variability associated with the GMPEs. Whereas the link between the seismological parameters and ground motion can be easily developed in the Fourier domain, engineering applications of predictive models deal often with response spectra (SA). Similarities and differences between Fourier amplitude spectra (FAS) and SA have been discussed since the early development of the SA concepts, and the impact of such differences on the host-to-target adjustments has been recently revised (Bora *et al*. 2016).

The aim of this study is two-fold: first, to construct seismological models for the area affected by the 2009 L'Aquila (Abruzzo region, central Italy) seismic sequence and to use such models for interpreting the different components of the aleatory variability associated with a GMPE developed for the same area; second, to compare the empirical models derived for Fourier with those derived for SA, discussing their differences in terms of captured ground motion variability. To pursue such aims, this work is structured in two parts: in the first part, entitled Seismological models, we refine the spectral model derived by Pacor *et al.* (2016) using the Generalized Inversion Technique (GIT; Andrews 1986; Castro *et al.* 1990; Oth *et al*. 2008) to extract the source, propagation and site amplification from the spectra of S-wave windows; in the second part, entitled Ground motion prediction equations, empirical GMPEs are derived both for the FAS and SA, and their residual distributions are evaluated. Finally, the outcomes of the GIT inversion are used to interpret the GMPE residuals in terms of seismological parameters.

## 2 DATA SET

The data set used in this study is composed by about 9000 waveforms from 231 earthquakes recorded by 148 stations in central Italy (Fig. 1), extracted from the data set analysed by Pacor *et al*. (2016) (hereinafter referred to as PAC16) and enriched by temporary stations installed after the main shock ($M_w$ 6.1, $M_L$ 5.9) of the 2009 L'Aquila sequence. The data set spans the time period from January 2008 to May 2013 and it is mostly populated with events of the L'Aquila sequence, which struck the Abruzzo region on 2009 April 6 (e.g. Ameri *et al.* 2009). It includes both velocimetric and accelerometric signals recorded by temporary and permanent stations of the National Seismic Network (RSN, Rete Sismica Nazionale) operated by INGV and by the national Accelerometric Network (RAN, Rete Nazionale Accelerometrica) operated by the Italian Civil Protection Department (DPC). For each event, the local magnitude is computed accordingly to Di Bona (2016) and the *P*- and *S*-wave onsets obtained by an automatic phase-picker (Spallarossa *et al*. 2016) are used to relocate the hypocentres using the regional 1-D velocity model reported in Valoroso *et al*. (2013). A final visual inspection is applied to verify the automatic arrival times and to discard clipped or distorted signals. The local magnitude varies in the range 2.9–5.9, with the bulk of data between 3.0 and 3.5, and the hypocentral distances up to 120 km are considered (Fig. 1). Additional details about the data distribution are provided in Supporting Information Fig. S1. We analyse the geometrical mean of the two horizontal components in the frequency range 0.4–25 Hz, selecting earthquakes recorded by at least eight stations and stations with at least eight recordings. The applied data processing is detailed in PAC16. Here, we briefly summarize the procedure to compute and select the spectral amplitudes. The velocimetric records are corrected for the instrumental response and filtered over the band 0.05–40 Hz, whereas the strong motion records are processed following the procedure proposed by Paolucci *et al.* (2011) and detailed in Pacor *et al.* (2011). We analyse time windows including mainly S-wave arrivals, starting 0.1 s before the estimated S-onset and ending when the cumulated energy reaches a fraction of the total one. The applied energy thresholds are distance-dependent: 90 per cent for distances $R < 25$ km; 80 per cent in the distance range 25–70 km; 70 per cent for $R > 50$ km. The minimum window length (Ts) is fixed to 4 s, the maximum is about 20 s and the median value is about 6 s (the distribution of Ts is shown in Supporting Information Fig. S1). To compute the FAS, the extracted time-windows are tapered (5 per cent) and the FAS smoothed using the Konno & Ohmachi (1998) algorithm with smoothing parameter b set equal to 40. Since the data set includes windows with Ts$<$ 5 s, for each record we consider spectral amplitudes at frequencies greater than 3/Ts. Furthermore, we select amplitudes with signal-to-noise ratio (SNR) above 10 (with respect to the spectra of the pre-event noise). Finally, only Fourier spectra having at least 70 per cent of frequencies above the selected SNR within the analysed frequency range are further considered for the analysis.

## 3 SEISMOLOGICAL MODELS FOR FOURIER AMPLITUDE SPECTRA

Following PAC16, we apply an inversion scheme to isolate the source, attenuation and site contributions to the observed ground motion. The inversion is performed in two steps: first, the three terms are separated employing a non-parametric inversion approach; then, standard seismological models are used to parametrize the source and attenuation functions obtained in the first step. Since the parametrization is applied only in the second step, the characteristics of the models chosen for describing each specific term are not affecting the results obtained for the other terms.

### 3.1 Non-parametric GIT inversion

The non-parametric GIT approach is used in this study to isolate the source, propagation and site contributions to the observed ground motion (Parolai *et al.* 2001; Bindi *et al*. 2004; Bindi *et al.* 2009, Pacor *et al*. 2016 for previous GIT applications in central Italy). For each frequency $f$, the FAS of *S*-wave windows relevant to earthquake $i$ recorded at station $j$ are expressed as:

$$\begin{aligned}\mathrm{Log}\left[\mathrm{FAS}_{ij}(f)\right] = {} & \mathrm{Log}\left[\mathrm{Source}_i(f)\right] \\ & + \mathrm{Log}\left[\mathrm{Attenuation}\left(R_{ij}, f\right)\right] \\ & + \mathrm{Log}\left[\mathrm{Site}_j(f)\right], \end{aligned} \quad (1)$$

where $R_{ij}$ is the hypocentral distance. When model (1) is applied simultaneously to several earthquakes recorded by a seismic network, an overdetermined system of linear equations is obtained that can be solved in a least squares sense (Paige & Saunders 1982). eq. (1) combines three different terms which show mutual trade-offs. In order to remove two unresolved degrees of freedom, additional constraints have to be considered (e.g. Castro *et al*. 1990). The first constraint is applied to the attenuation function by requiring that it assumes a given value at a fixed reference distance. We set the attenuation to 1 at the reference distance of 5 km (i.e. *Attenuation*$(5,f) = 1$, irrespective of the frequency). The second constraint is applied to the site term, selecting some stations as reference. Although the trade-off between source and site is removed by this constraint, amplification/attenuation characteristics common to all reference stations may be transferred to the source (Oth *et al*. 2011),

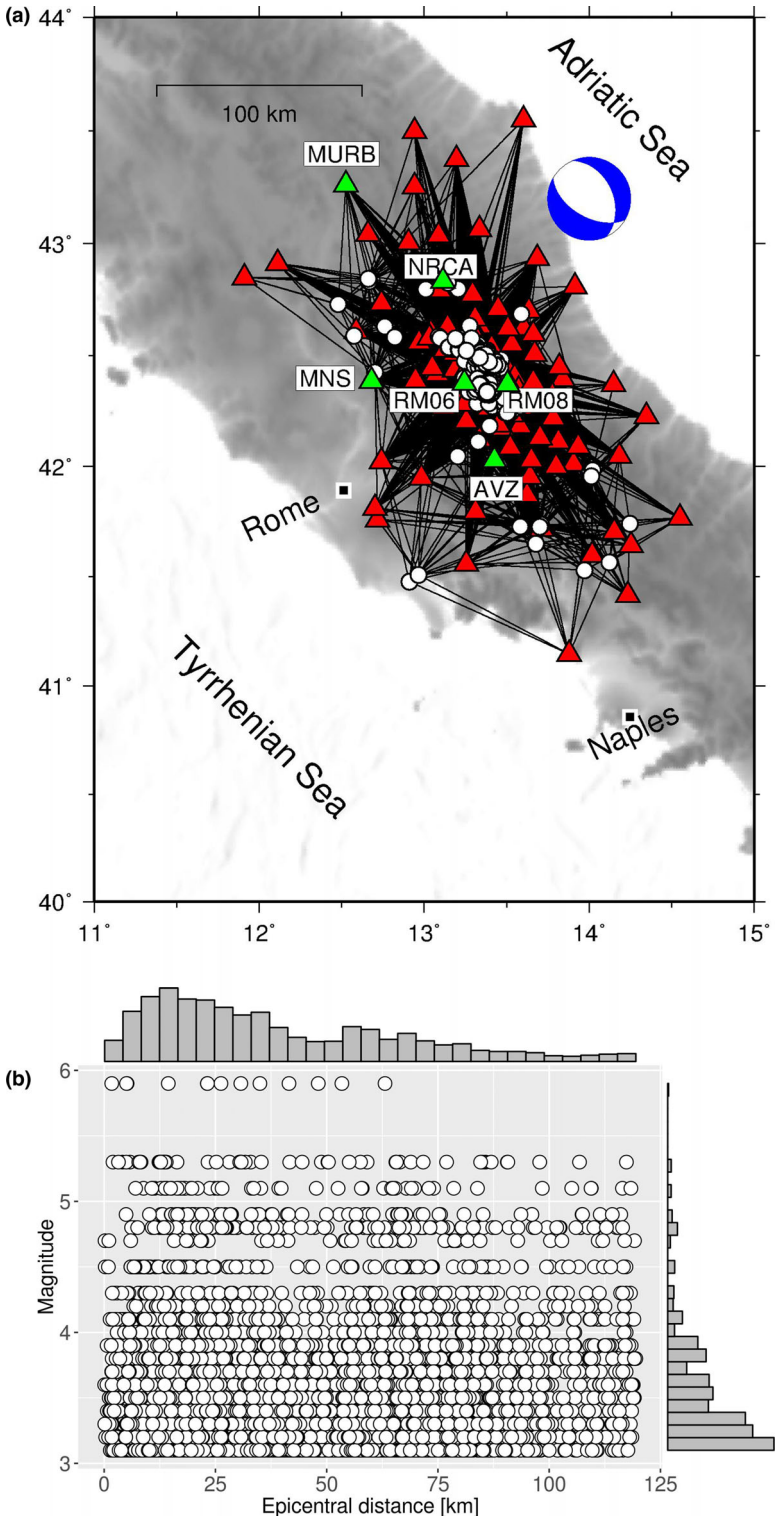


**Figure 1.** (a) Path coverage, station locations (triangles) and earthquake epicentres (circles) of Abruzzo data set. The focal mechanism of the 2009 L'Aquila main shock ($M_w$ 6.1) is indicated by its beach ball. Green triangles indicate stations mentioned in the text. (b) Local magnitude versus epicentral distance scatter plot.

making critical the choice of the reference stations. We consider two alternative site constraints defined by:

$$\text{Reference condition A}: \sum_{j=1}^{N_{sta}} \text{Log}\left[\text{Site}_j(f)\right] = 0 \quad (2)$$

$$\text{Reference condition B}: \sum_{j} \text{Log}\left[\text{Site}_j(f)\right] = 0 \text{ for } j \in \Omega \quad (3)$$

where $\Omega$ is the set of indexes corresponding to selected reference stations and $N_{sta}$ is the total number of selected stations. The amplification functions inferred adopting either eq. (2) or (3) may be

different. The first case provides results relative to the average site amplification of the whole network (which, depending on the characteristics of recording sites, can be affected by significant amplification effects) while, in the second case, the amplification functions are relative to one or to a set of rock sites assumed to have, on average, a flat site response. The site reference condition has little effect on the attenuation term for well-balanced data sets (Oth *et al.* 2011) while the source and site amplification curves depend on the chosen site reference condition. In the following GIT inversions, we consider eq. (2) for computing the site terms to be compared with GMPE results while eq. (3), which minimizes the bias on source spectra related to site effects, is applied to assess the source parameters. As references sites, we select the same set considered by PAC16, namely stations MNS, RM06, RM08 (Fig. 1).

### 3.2 Parametric models

The non-parametric functions obtained by solving eq. (1) are described in terms of standard seismological models to infer the parameters relative to source and attenuation models. The revision of PAC16 results is mainly motivated by the decision of applying different parametric models, as well as to consider both the moment and local magnitudes.

The attenuation functions are parametrized in terms of geometrical spreading attenuation $G(R)$, frequency-dependent quality factor $Q(f)$ and frequency-independent kappa ($k$) parameter as follows:

$$\text{Attenuation}\ (f, R) = \begin{cases} G(R)\exp\left[-\dfrac{\pi f (R-R_0)}{Q_o f^{\alpha} v_s}\right] & for\ f \le f_0 \\ G(R)\exp\left\{-\pi\left[\dfrac{(R-R_0)}{Q_o f^{\alpha} v_s} f + \chi(R)\, k\,(f-f_0)\right]\right\} & \text{otherwise} \end{cases} \tag{4}$$

where $R_0$ is the reference distance used in the GIT inversion (i.e. 5 km in our application), and $\chi(R)$ is a cosine-taper function increasing from 0 at 5 km to 1 at distances larger than 20 km (the tapering is applied to preserve the constraint on distance, i.e. $A(f,5)= 1$). The kappa ($k$) parameter, applied for frequencies larger than a threshold frequency $f_0$, allows us to account for a regional, frequency-independent attenuation effect common to all ray paths. The frequency $f_0$, selected above the range spanned by the source corner frequencies, is set to 10 Hz. Following PAC16, the geometrical spreading is parametrized with a tri-linear piece-wise function (e.g. Atkinson 2004; Malagnini *et al.* 2011), defined as

$$G(r) = \begin{cases} \left(\dfrac{r_0}{r}\right)^{n_1}, & \text{for } r \le 10 \text{ km} \\ \left(\dfrac{r_0}{10}\right)^{n_1}\left(\dfrac{10}{r}\right)^{n_2}, & \text{for } r > 10 \text{ km and } r \le 65 \text{ km} \\ \left(\dfrac{r_0}{10}\right)^{n_1}\left(\dfrac{10}{65}\right)^{n_2}\left(\dfrac{65}{r}\right)^{n_3}, & \text{for } r \ge 65 \text{ km} \end{cases} \tag{5}$$

where the hinge distances at 10 and 65 km are selected after performing preliminary trial and error regressions. The best least-squares solution corresponds to [n1; n2; n3] = [1.05 ± 0.01; 1.76 ± 0.03; 0.68 ± 0.03], similar to the values obtained by PAC16. Then, by inserting the obtained G(R) in eq. (4), the values of $Q_0$, $\alpha$, and $k$ are estimated through a least-square regression. The best fit model is given by:

$$Q(f) = (239 \pm 3)\ f^{(0.16\pm0.01)} \tag{6}$$

$$k = (0.0105 \pm 0.0006)\ [s], \tag{7}$$

where the 95 per cent confidence intervals for the parameters are indicated. The residuals between the non-parametric attenuation values and the predictions from the parametric models defined by eqs (5)–(7) are shown in Supporting Information Fig. S2. The population has zero mean and standard deviation equal to 0.09 in $\log_{10}$ units (panel a), indicating that on average the parametric models well describe the empirical attenuation curves, although distances larger than 90 km show some peculiar trends with frequency (panel b).

The non-parametric source curves obtained solving eq. (1) with reference condition B (eq. 3), are described in terms of the Brune (1970) model, defined as:

$$\text{Source}\ (f) = \frac{\Re_{\theta\varphi} F V}{4\pi\rho {v_s}^3 R_0}\, M_0 (2\pi f)^2 \frac{1}{1+\left(\frac{f}{f_c}\right)^2} \tag{8}$$

where $v_s$ is the shear wave velocity, $R_0$ is the reference distance; $M_0$ denotes the seismic moment and $f_c$ is the corner frequency; $\Re_{\theta\varphi}$ is the average radiation pattern for $S$-waves, set to 0.55; $V = 1/\sqrt{2}$ is the partition of $S$-wave energy into the two horizontal components; $F = 2$ is the free-surface amplification and $\rho = 2800$ kg m$^{-3}$ is the density. Once eq. (8) is fit to the non-parametric spectral source functions, the Brune stress drop is computed as (Keilis-Borok 1959; Brune 1970)

$$\Delta\sigma = \frac{7 M_0}{16 r^3}, \tag{9}$$

where the source radius $r$ is given by

$$r = \frac{2.34 \cdot v_s}{2\pi f_c}. \tag{10}$$

The non-parametric source functions are shown in Fig. 2(a) and (b), considering the reference condition A (eq. 2) and B (eq. 3). In applying eq. (2), the average high frequency attenuation affecting the stations of the network is transferred to the source, as confirmed by comparing the average slope of the source spectra for the two cases (Fig. 2c). The average slopes are 0.013 and 0.00 s (standard deviation 0.010 s) for reference condition A and B, respectively. To estimate the source parameters by fitting the Brune's model, the spectra obtained by performing the GIT inversion with the constraint given by eq. (3) are considered. The distribution of the corner frequencies is shown in Supporting Information Fig. S3 while the $\Delta\sigma$ estimated from the corner frequencies are shown in Fig. 3 as function of local and moment magnitudes (see Supporting Information Fig. S4 for a comparison between $M_L$ and $M_w$). Although a detailed discussion on the source scaling is beyond the aim of this work, we calibrate two parametric models for the stress drop as function of magnitude and depth (e.g. Yeneir & Atkinson 2015a): the first model considers local magnitude whereas the second one adopts the moment magnitude. The best fit models are given by:

$$\log[\Delta\sigma(ML, h)] = \begin{cases} -1.6902 + 0.6097 ML + \gamma_{\text{hl}} & \text{for } M < 5 \\ 1.3585 + \gamma_{\text{hl}} & \text{otherwise} \end{cases} \tag{11}$$

$$\log[\Delta\sigma(M_w, h)] = \begin{cases} 0.3682 + \gamma_{\text{hw}} & \text{for } M < 4.2 \\ 0.3682 + 1.1430(M_w - 4.2) + \gamma_{hw} & \text{for } 4.2 \le M < 5 \\ 1.2825 + \gamma_{\text{hw}} & \text{otherwise} \end{cases} \tag{12}$$

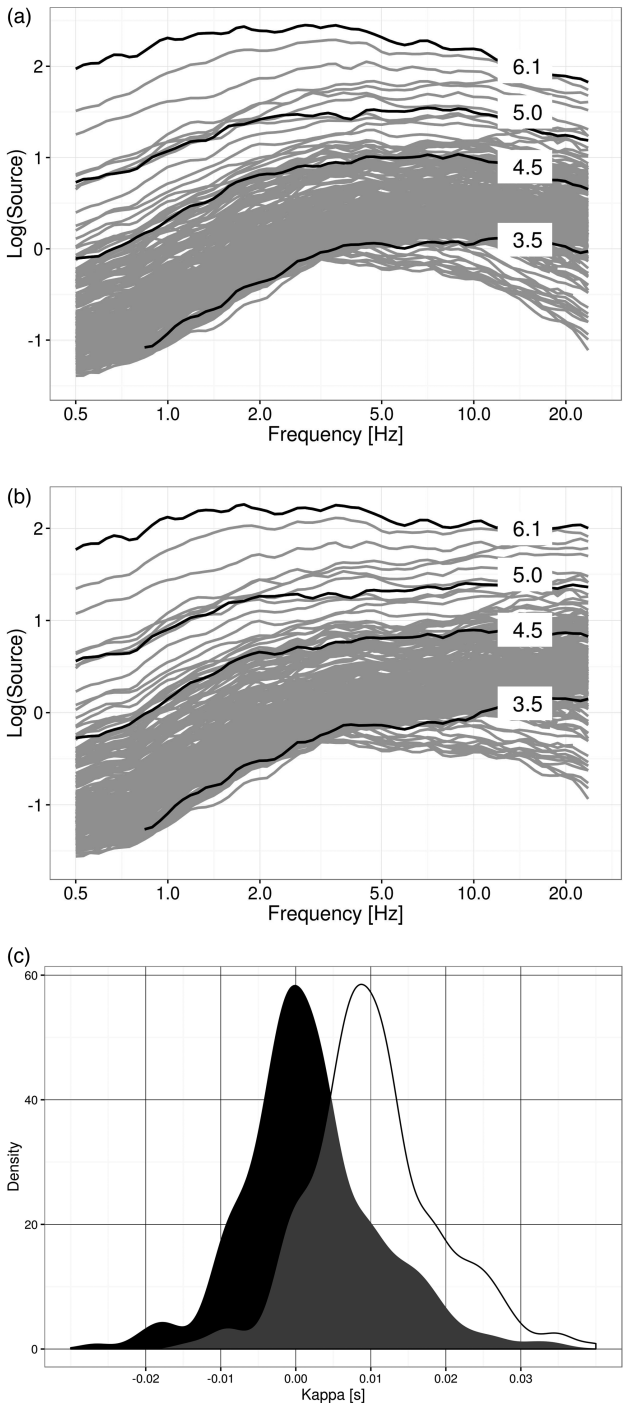


**Figure 2.** Non-parametric Fourier source spectra obtained by applying to GIT the constraints given in eqs(2) (panel a) and (3) (panel b). The spectra of few events with different magnitudes are shown in black. The distributions of the slopes of the high frequency spectral values (estimated starting from 10 Hz) are shown in panel (c), considering the results of panels (a) (transparent distribution) and (b) (black distribution).

where $\gamma_{hl}$ is a depth-dependent adjustment offset equal to $-0.1198$ for depths $h$ shallower than 8 km, and equal to 0.1198 for $h \geq 8$ km when $M_L$ is considered; considering $M_w$, the depth-dependent adjustment is $\gamma_{hw} = \pm 0.14477$. The model describing the stress drop dependence on moment magnitude (eq. 12) shows an overall agreement with several evidences observed for other regions such as California or Central East North America (CENA; Yener &

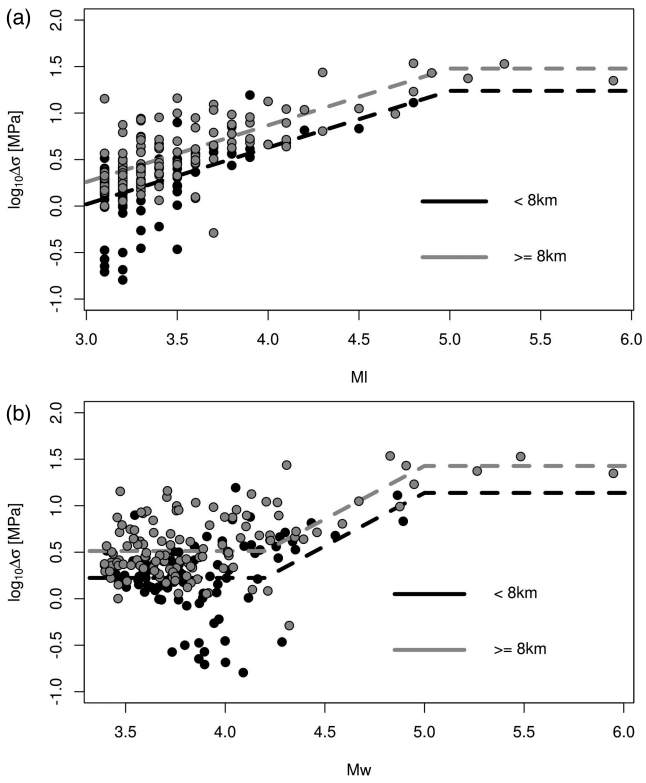


**Figure 3.** Models for stress drop $\Delta\sigma$ as function of local magnitude (a) and moment magnitude (b). Events with hypocentral depth shallower than 8 km are shown in black, those with deeper hypocentral depth in grey. The dashed lines show the calibrated models for the two depth ranges (eqs 11 and 12).

Atkinson 2015a,b). For example, these models show an increase of the stress drop with magnitude and saturate above a given magnitude threshold (see Supporting Information Fig. S5). The tendency of stress drop to increase with depth is also captured by the models derived for different regions. The models in eq. (11) and (12) are used in the next sections for analysing the ground motion variability.

## 4 COMPARISON BETWEEN FOURIER AND RESPONSE SPECTRA

In this section, we apply the GIT approach to acceleration SA (5 per cent damping), following the common practice in engineering seismology to develop GMPE describing the logarithm of SA as sum of terms related to source, propagation and site. Indeed, since the response spectrum is not a linear function of the input motion, it is not straightforward that we can provide any seismological interpretations to the GIT results for SA. The connection between the response spectrum and the Fourier amplitude spectrum can be explained using the Random Vibration Theory (e.g. Bora *et al.* 2016 and references therein). As detailed in Bora *et al.* (2016), the response spectrum can be computed, to a first approximation, as the square root of the zeroth order moment of the oscillator response (e.g. see Fig. 1 in Bora *et al.* 2016), that is:

$$\mathrm{SA}(f_{\mathrm{osc}}, \xi) \sim \left[2 \int_0^{\infty} |\mathrm{Source}(f)\mathrm{Attenuation}(f)\mathrm{Site}(f) I_{\mathrm{oscillator}}(f; f_{\mathrm{osc}}, \xi)|^2 \mathrm{df}\right]^{1/2}, \quad (13)$$

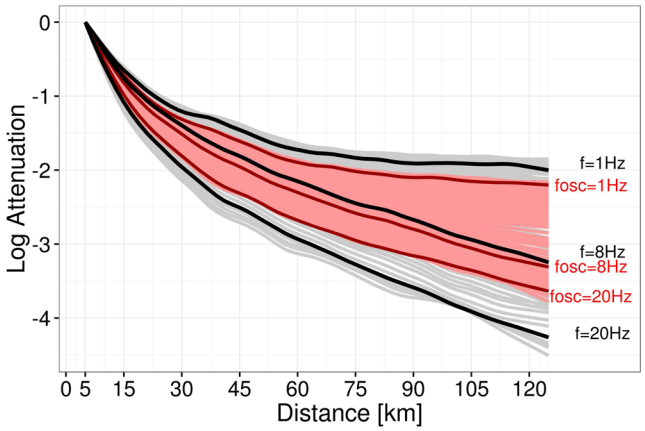


**Figure 4.** Comparison between non-parametric attenuation curves derived from FAS (grey) and SA (light red), for different frequencies. Attenuation curves for FAS at $f = 1, 8, 20$ Hz are shown in black, attenuation curves for SA at $f_{osc} = 1, 8, 20$ Hz are shown in dark red.

where $I_{oscillator}(f; f_{osc}, \xi)$ is the transfer function of a single degree of freedom oscillator (SDOF) with resonance frequency $f_{osc}$ and damping $\xi$. In comparing the results from FAS with SA, we should therefore take into consideration the transfer function of the oscillator and the integration as shown in eq. (13).

Fig. 4 shows the non-parametric attenuation curves obtained for FAS and SA. The attenuation curves for SA span a narrower amplitude range than FAS. In particular, the attenuation for SA shows little variation for frequencies $f_{osc}$ above 10 Hz and below 1 Hz, approximately. This result can be explained using eq. (13) along with the following considerations: (i) almost all the source corner frequencies of the analysed earthquakes lie between 1 and 10 Hz (Supporting Information Fig. S3); (ii) the ground motion at high frequencies is attenuated by $Q$ and $k$; (iii) the transfer function of the SDOF is flat below the resonance frequency and it filters out the signal at frequencies above the resonance. Therefore, when $f_{osc}$ lies in the range 1–10 Hz (i.e. within the flat part of the input acceleration spectrum), the response of the SDOF is dominated by the input motion for frequencies around $f_{osc}$; when $f_{osc}$ is large enough to correspond to frequencies attenuated by $Q$ and $k$, the contribution of the input at frequencies around $f_{osc}$ becomes negligible and the response of the SDOF is mainly controlled by the integral in eq. (13) over the flat response of the SDOF; for $f_{osc}$ low enough (i.e. below the corner frequency of the earthquake), the response of the SDOF has small acceleration (indeed, for small $f_{osc}$, displacement response of the SDOF would be more informative). It follows that SA does not depend on $f_{osc}$ when $f_{osc}$ is large enough to coincide with the frequency of harmonics strongly attenuated in the acceleration input spectrum. This causes a saturation effect that is clearly visible in the attenuation curves shown in Fig. 4. To better exemplify the comparison between GIT results for FAS and SA, Fig. 5 shows the observed spectra, the spectral attenuation curves and the site terms for a $M_w$ 4.6 earthquake recorded at the stations highlighted in Fig. 1: AVZ (hypocentral distance $R_{hypo} = 40$ km), MURB ($R_{hypo} = 119$ km), and NRCA ($R_{hypo} = 55$ km). In panel (a), while FAS is affected by the high frequency attenuation (anelastic attenuation and kappa effects), SA is flat at high frequencies, and converges to the peak ground acceleration recorded at each site. The extracted site terms for FAS and SA (panel b) have similar shapes at short and intermediate frequencies, but they differ at high frequencies, where SA is

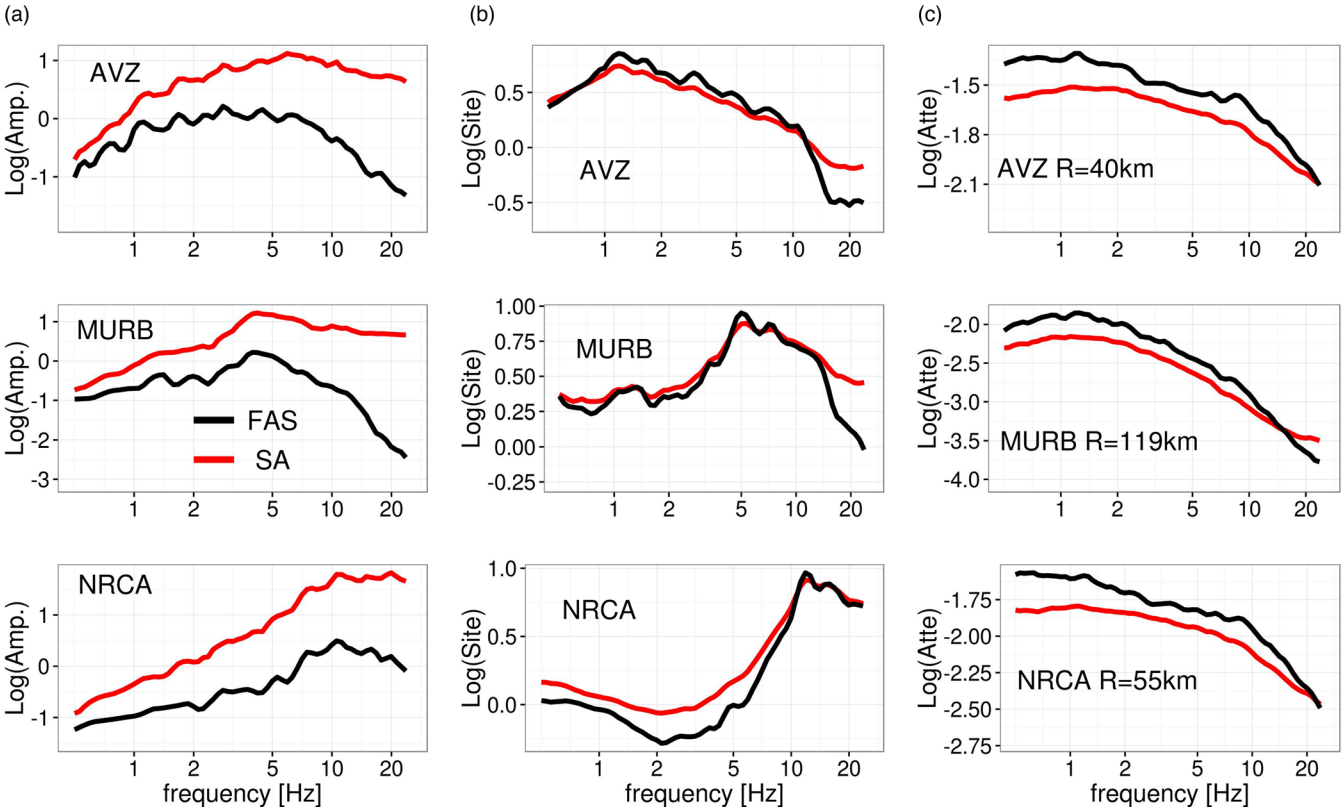


**Figure 5.** (a) Acceleration Fourier and response spectra (a), site amplification functions (b), attenuation functions (c) at stations AVZ (top), MURB (middle) and NRCA (bottom) for an $M_w = 4.6$ earthquake. The hypocentral distance $R$ of each station is provided in the right panel. Black lines are relative to FAS, red lines to response spectra.

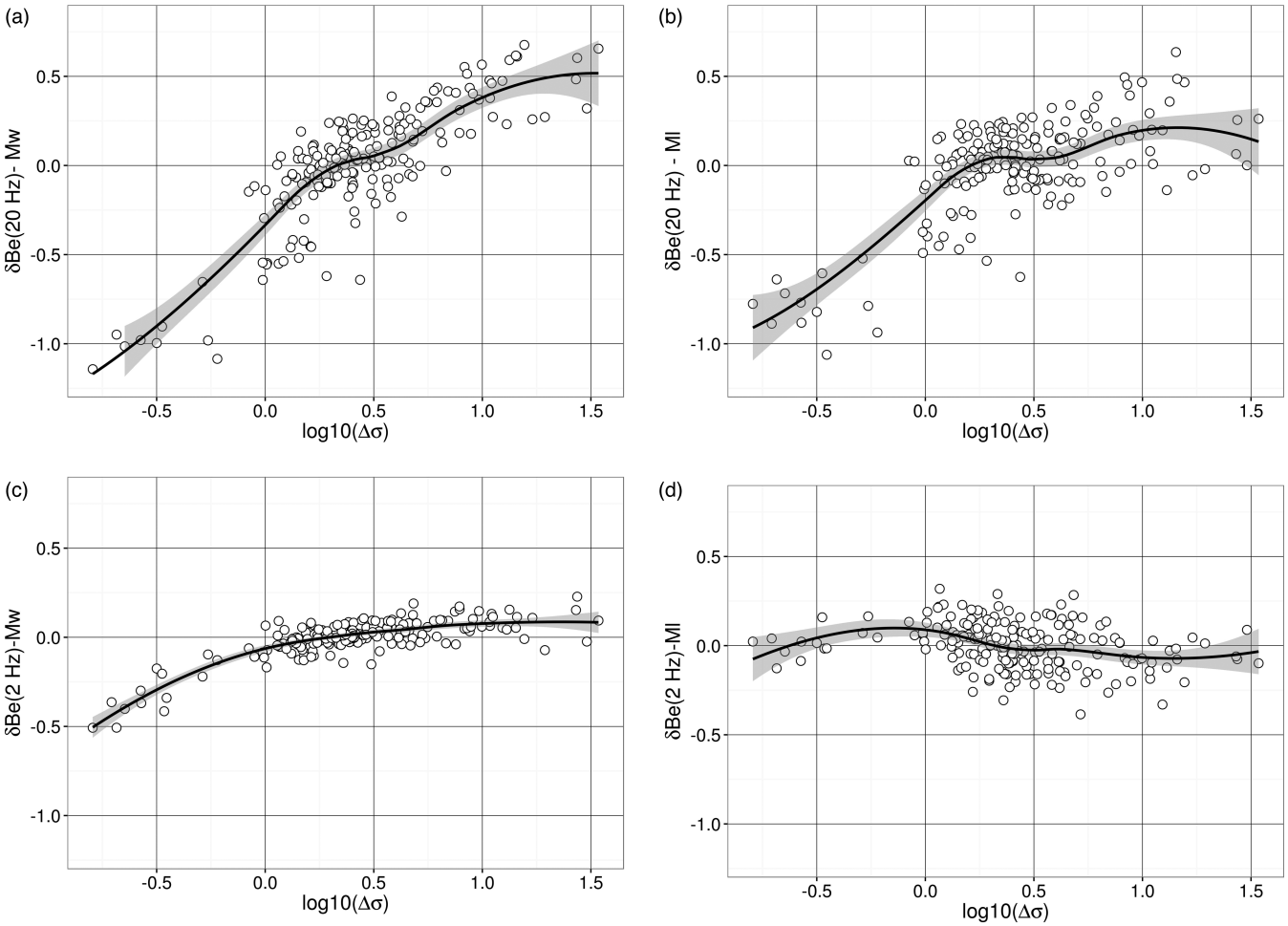


**Figure 6.** Between-event residuals for Fourier amplitudes versus stress drop at 20 Hz (a and b) and 2 Hz (c and d) considering $M_w$ (a and c) and $M_L$ (b and d) as explanatory variable. The trend lines are shown in black along with their $\pm 1$ standard deviation (grey area).

controlled by the overall input spectra. Only at station NRCA, the large amplification occurring at high frequencies allows to extend the frequency range where the oscillator response is controlled by frequencies around the resonance. Regarding the attenuation with distance (panel c), the results for FAS and SA show similar trends at low frequencies; at high frequencies, FAS attenuates faster than SA. Since $R_{hypo}$ is larger for station MURB than for stations AVZ and NRCA, the high frequency attenuation is stronger for the MURB recording and the crossing between FAS and SA occurs at lower frequencies (about 15 Hz) with respect to the crossing for AVZ and NRCA.

## 5 GROUND MOTION PREDICTION EQUATIONS

We develop a GMPE using the Abruzzo data set applying a random effect approach (Abrahamson & Youngs 1992; Bates *et al.* 2015; Kotha *et al.* 2016)

$$\log(Y) = e_1 + e_2(M - M_{ref}) + e_3 \log\left(\frac{R_{hypo}}{R_{ref}}\right) + e_4\left(R_{hypo} - R_{ref}\right) + \delta B_e + \delta S2S + \delta WS \quad (14)$$

where $Y$ is either the amplitude of the FAS at frequency $f$ or the SA at the frequency oscillator $f_{osc}$; $M_{ref}$ is the reference magnitude set equal to 4; $R_{ref}$ is the reference distance set equal to 5 km. The GMPE is calibrated for both local ($M_L$) and moment ($M_w$) magnitudes, and using the hypocentral distance $R_{hypo}$. eq. (14) contains three random effects: $\delta B_e$ is the between-event distribution which measures the systematic deviation from the median of each group of recordings for the same event; $\delta$S2S is the between-station residual distribution measuring the systematic deviation from the median of the recordings relevant to the same station; $\delta$WS is the single-station within-event residual (see Al Atik *et al.* 2010 for a complete glossary of terms describing the components of the ground motion variability in the framework of probabilistic seismic hazard assessment). Since no site term is included in the median, the between stations are expected to provide a non-parametric description of the linear site effects. In this study, we focus on $\delta B_e$ and $\delta$S2S residuals and on their connection with the seismological parameters derived in the previous section.

Fig. 6 shows $\delta B_e$ as function of the stress drop $\Delta\sigma$ for two frequencies, considering FAS. The between-event residuals show a clear dependence on the stress drop at high frequencies; this dependence is weaker, and the data are more scattered, for $M_L$ (panel b) than for $M_w$ (panel a). On the contrary, at low frequencies, $\delta B_e$ is almost independent of $\Delta\sigma$ (panel d) except for low stress-drop values ($\Delta\sigma < 1$ MPa) in the model implementing $M_w$ (panel c). Similar results are obtained for SA, as shown in Supporting Information Fig. S6.

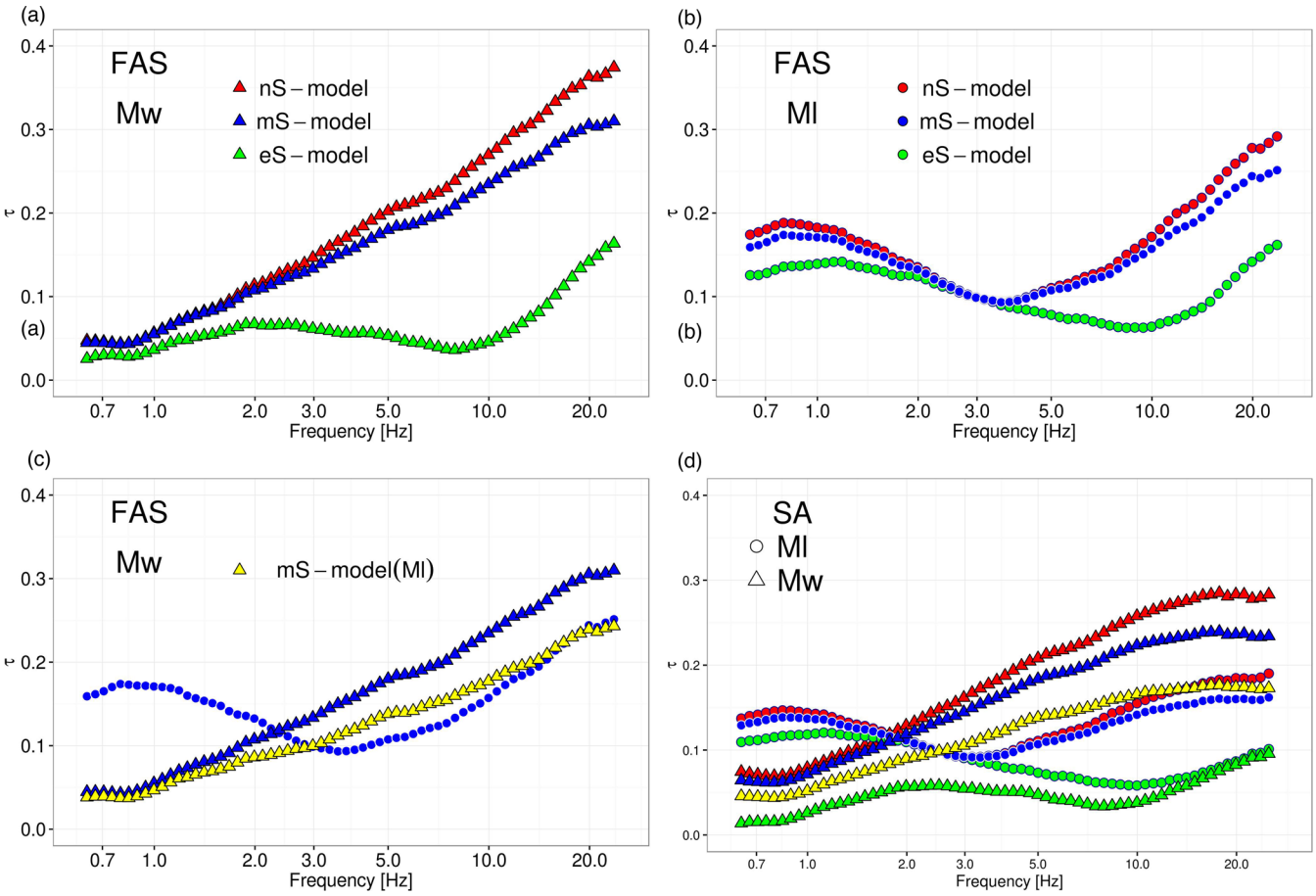


**Figure 7.** Frequency dependence of the standard deviation $\tau$ of the between-event residuals. Circles: results for $M_L$; triangles: results for $M_w$. Red symbols: nS-model, not including the stress drop $\Delta\sigma$; green symbols: eS-model, including the $\Delta\sigma$ estimated for each earthquake; blue symbols: mS-model, including $\Delta\sigma$ computed through the empirical relationships in eqs (11) and (12); yellow: results for the GMPE using $M_w$ but applying the mS-model calibrated over $M_L$ (eq. 11). (a) Results for Fourier spectra considering $M_w$; (b) results for Fourier spectra (FAS) considering $M_L$; (c) the FAS results for $M_w$ using eq. (11) to model $\Delta\sigma$ (blue triangles, the same as in panel a) are compared to those obtained using eq. (12) (yellow) and to the results obtained for $M_L$ in panel (b) (blue circles); (d) results obtained for spectral acceleration (SA).

The trends shown in Fig. 6 highlight a close relationship between stress drop and ground motion variabilities at high frequencies, as expected by the classical source theory. Therefore, the regression is repeated introducing the stress drop $\Delta\sigma$ in the functional forms

$$\log\ (Y) = e_1\ + e_2\,(M - M_{\rm ref}) + e_3 \log\left(\frac{R_{\rm hypo}}{R_{\rm ref}}\right) + e_4\left(R_{\rm hypo} - R_{\rm ref}\right) + e_5 \log\Delta\sigma + \delta {\rm B_e} + \delta {\rm S2S} + \in . \qquad (15)$$

Separate regressions are performed for $M_w$ and $M_L$. For each magnitude scale, different models are developed: (i) eS-model, which implements the empirical $\Delta\sigma$ values inferred by the GIT for each earthquake; (ii) mS-model, which adopts the $\Delta\sigma$ values estimated through the models given by eq. (11) and (12) for $M_L$ and $M_w$, respectively. The regression not including the stress drop in the functional form (eq. 14) is referred to as nS-model. Fig. 7 compares the frequency dependence of $\tau$ for FAS and SA, considering the different models described above: (i) GMPEs without stress drop (nS-model, red symbols); (ii) GMPEs including stress drops estimated by GIT (eS-model, green symbols); (iii) GMPEs including stress drops modelled through eqs (11) and (12) (mS-model, blue symbols). The between-event variability of FAS strongly reduces for eS-model, both for $M_w$ (panel a) and $M_L$ (panel b), in comparison to model without $\Delta\sigma$ as explanatory variable (nS-model). For $M_w$, $\tau$ is smaller than 0.1 up to 15 Hz, and the reduction at 10 Hz is of about 80 per cent (i.e. from 0.27 to 0.05). The results for $M_L$ (panel b) are similar but the overall reduction is smaller than for $M_w$. $\tau$ decreases at frequencies lower than about 2 Hz (where the Wood-Anderson filters the data) and above 3 Hz, reaching a reduction of about 60 per cent at 10 Hz (i.e. from 0.17 to 0.07).

While introducing the empirical estimates of the stress drop in the GMPEs allows us to quantify its impact on the overall variability, the resulting model has a limited applicability for prediction purposes. Therefore, the stress drop is introduced through regional models, such those in eqs (11) and (12), connecting $\Delta\sigma$ to proxies like magnitude and depth (see also Yener & Atkinson 2015a,b). For mS-model (Fig. 7, blue symbols), $\tau$ decreases at high frequency (>2 Hz) when $M_w$ is considered (panel a) while there is a small improvement for $M_L$.

Finally, we test the impact of introducing the regional stress drop model depending on $M_L$ (eq. 11) into the GMPE calibrated for $M_w$ (yellow symbols in panel c). It is worth noting that in this case both $M_w$ and $M_L$ appear as explanatory variables of the GMPE, providing a connection with source characteristics over a wide frequency range (Atkinson 1995; Atkinson & Hanks 1995). The comparison shown in panel c of Fig. 8 confirms that $\tau$ of this hybrid model is the lowest, combining the benefits of using $M_w$ at low frequency and $M_L$ at high frequency.

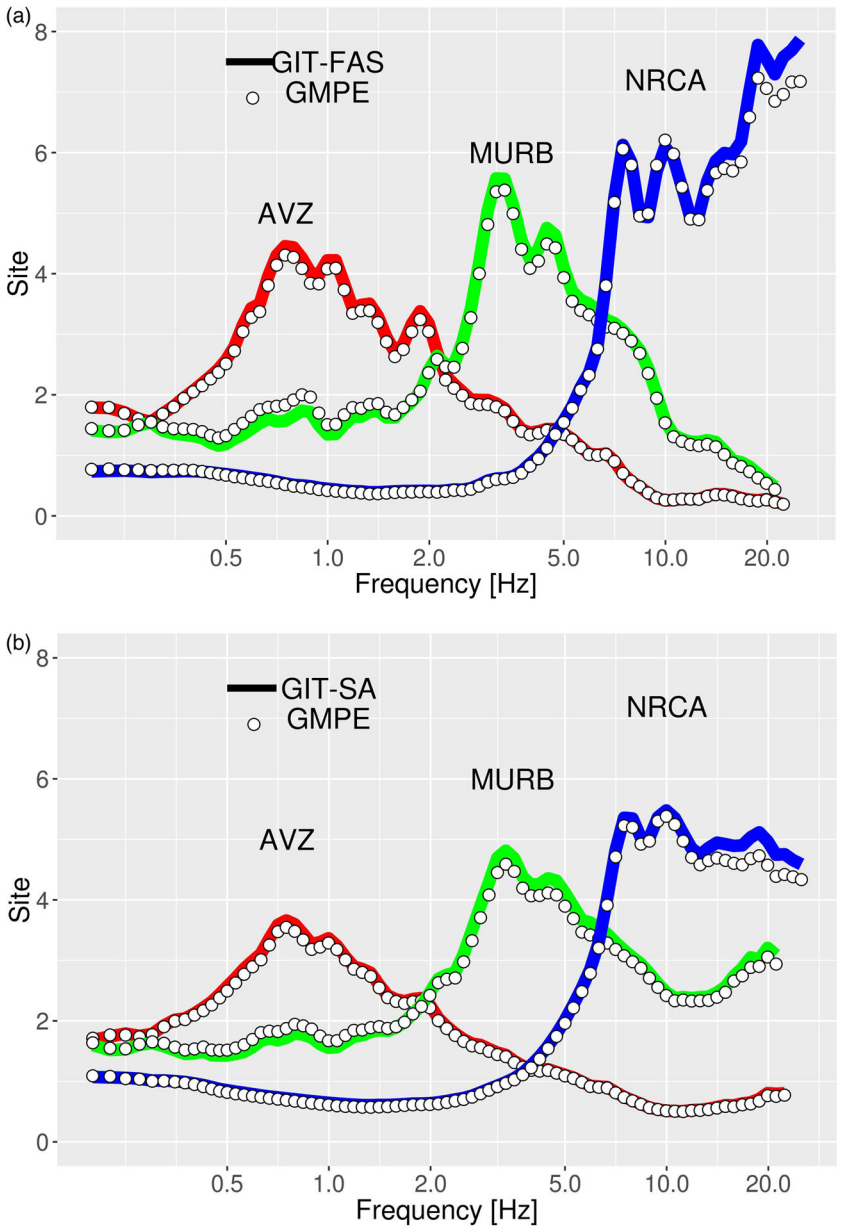


**Figure 8.** $\delta$S2S (circles) and GIT amplifications (continuous lines) for FAS (a) and SA (b), considering three stations (red: AVZ; green: MURB; blue: NARCA).

The results for SA (Fig. 7d) depict similar trends, although $\tau$ is generally smaller than for FAS. In particular, considering the nS- and mS-models, $\tau$ shows a saturation effect starting from about 8 Hz, whereas the results for FAS show an almost linear trend with the logarithm of frequency. These trends confirm that SA is less effective in capturing the high-frequency variations in the input ground motion than FAS.

The site amplification retrieved by the GIT inversion can be compared to the between-station residuals, that is, $\delta$S2S. Fig. 8 exemplifies the comparison for three stations (i.e. AVZ, MURB, and NRCA) which amplify the ground motion over different frequency bands: AVZ (Avezzano) is installed within a large alluvial basin about 40 km southern than L'Aquila, over about 180 m of sediments with vs30 = 199 m $s^{-1}$, and shows a fundamental frequency of resonance at 0.75 Hz(ESM working group 2015); MURB (Monte Urbino) is classified as soil category B accordingly to EC8 (i.e. vs30 in the range 360–800 m $s^{-1}$) and it is installed on the crest of a gentle topography, with a peak of amplification at 3 Hz; NRCA (Norcia), also site class EC8-B, is installed in a narrow valley, at the base of a steep hill, with a fundamental frequency of resonance at 7 Hz (ESM working group 2015). Fig. 8 shows that there is a good agreement between $\delta$S2S (circles) and GIT site amplifications, confirming that $\delta$S2S can be used as empirical linear site amplifications. It is worth noting that the GIT results for FAS and SA show differences mainly in the high frequency range and in the overall amplification levels.

Finally, Fig. 9 compares the non-parametric attenuation curves with the distance scaling of the GMPE considering the results for 1, 10 and 20 Hz (blue curves). As previously discussed (eq. 5), the attenuation with distance can be described with a tri-linear geometrical spreading model, with hinge distances at 10 and 65 km (eq. 5). Since in the GMPE the coefficient for the log-distance term is distance-independent (i.e. coefficient $e_4$ in eqs 16 and 17), the GMPE scaling is mainly controlled by the attenuations at intermediate distances, leading to an over-estimation of the attenuation at short distances. The scaling with frequency is well captured and for low-frequency (i.e. 1 Hz in Fig. 9), the positive values

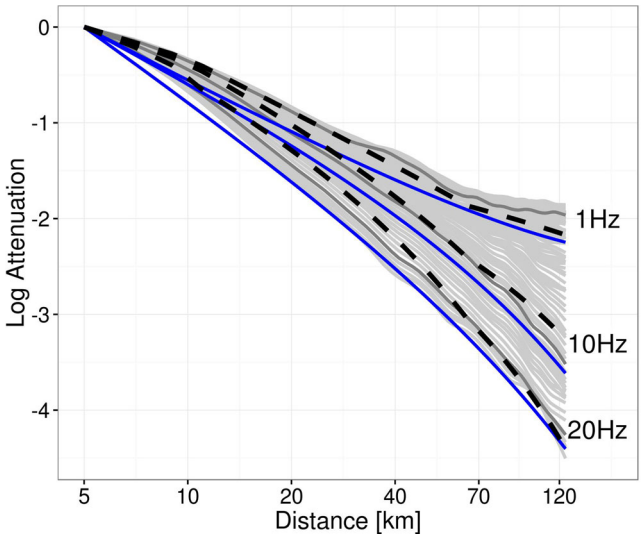


**Figure 9.** Comparison between GIT parametric attenuation curves for FAS at 1, 10 and 20 Hz (black dashed) and distance scaling of the calibrated GMPE (blue) for the same frequencies. The grey lines show the non-parametric GIT attenuation curves for the whole set of analysed frequencies.

assumed by the coefficient for the linear attenuation with distance (i.e. coefficient $e_5$ in eq. 15) allows to capture the flattening of the non-parametric curves for distances larger than 70 km.

## 6 DISCUSSION

The between-event residuals ($\delta B_e$) for the FAS show a clear dependence on the Brune's stress drop ($\Delta\sigma$) as computed from the corner frequency and seismic moment of the source spectra (Fig. 6). The impact of the stress drop variability over the between-event variability has been invoked and discussed in several publications. For example, Youngs *et al.* (1995) suggested the reduction of the stress drop variability with increasing magnitude as a possible explanation for the reduction of the PGA between-event variability with increasing magnitude. The variability of $\Delta\sigma$ for small magnitude earthquakes has been also mentioned by Boore *et al.* (2014) as one of the possible causes for the bump shown by the standard deviation $\tau$ around 0.08 s. Bindi *et al.* (2007) highlighted a clear dependence of $\delta B_e$ on $\Delta\sigma$ for the aftershocks of the 1999 Izmit sequence (Turkey). The connection between $\Delta\sigma$ estimated from spectral analysis (i.e. through the evaluation of the corner frequency and seismic moment) and $\delta B_e$ of PGA has been discussed by Cotton *et al.* (2013), finding a significant discrepancy between the range of variability expected from the source parameters and the variability implied by the GMPE. Recently, Ameri *et al.* (personal communication) studied the dependence of $\delta B_e$ on $\Delta\sigma$ for small earthquakes that occurred in France and Switzerland, whereas Oth *et al.* (2015) performed a similar analysis for a large data set of earthquakes occurred in Japan. Both studies highlighted the importance of correctly accounting for regional variability in the average stress drop when interpreting the between-events dependency on this parameter.

While the between-event residuals show a dependence on the stress-drop, their variability depends on the magnitude scale used in the GMPE. Fig. 7 shows that for frequencies lower than 2 Hz, the standard deviation $\tau$ of the between-event residuals for the GMPE implementing $M_w$ is smaller than using $M_L$ while above 2 Hz the opposite is true. Then, for the analysed data set, $M_L$ better captures the source-related ground motion variability at intermediate frequencies when small to moderate earthquakes are analysed, in agreement with the results of Bindi *et al.* (2007) in northwestern Turkey. Recently, Mereu (2017) showed that, under some assumptions about the independence of the coda shape on the magnitude, $M_L$ is approximating the energy magnitude Me (Dineva & Mereu 2009). The linear scaling between $M_L$ and Me has been also discussed by Kanamori *et al.* (1993). This makes $M_L$ a good indicator for capturing the differences in the high-frequency spectral content among different earthquakes. On the other hand, the scaling between $M_w$ and Me depends on the scaling constant $\alpha$ of the seismic moment Mo with the characteristic fault dimension L (i.e. Mo scales as $L^{\alpha}$, with $\alpha = 3$ for self-similar earthquakes). When the earthquakes in the analysed region are characterized by different scaling constants $\alpha$, the $M_w$ versus Me (or $M_L$) relation spreads from a linear trend to a linear cluster (Mereu 2017). In such a case, while the average ratio between $M_w$ and Me is expected to be close to one, $M_w$ is not describing the variability in the high frequency spectral content (i.e. a linear cluster with a larger spread along the Me axis indicates that a wide range of Me can be associated with similar $M_w$ values). We observe in Fig. 10 that the between-event variability correlates well with the magnitude residual $\Delta M = M_w$-$M_L$ (corrected for the average difference $\overline{\Delta M}$ ), which can be used as an indicator for the difference between the size (i.e. controlled by the seismic moment) and strength (i.e. controlled by the radiated energy) of the earthquakes (Di Giacomo & Bormann 2011). The correlation is stronger at high frequency (20 Hz in Fig. 10); at lower frequencies (e.g. 2 Hz), although the between-event variability decreases, still the largest negative $\delta B_e$ values are associated with the largest negative $\Delta M$ residuals. The linear scaling between $M_w$ and $M_L$ for a perfect elastic medium has been also recently demonstrated theoretically by Deichmann (2017), provided that the stress drop and the rupture velocity do not vary systematically with seismic moment. The author, also, has investigated the impact of the attenuation in the medium, of the stress drop variability and of the influence of the Wood-Anderson on the scaling between $M_L$ and $M_w$. Remarkably, Deichmann has shown that the local magnitude is related to physical properties of the earthquake source, in particular seismic moment, stress drop and apparent rupture velocity, providing a theoretical support for the results obtained in this study.

For typical prospective applications (e.g. for hazard studies), empirical estimates of $\Delta\sigma$ computed for each earthquakes cannot be included in the GMPE, since the stress drop of future earthquakes cannot be predicted accurately. Recently, Yenier & Atkinson (2015a) introduced a host-to-target approach where a GMPE calibrated over numerical simulations performed in a region rich of data is applied to a target region by empirically adjusting key model parameters. For example, in their application to CENA, the authors assumed that the stress parameter (acting on the source spectrum similarly to the Brune's stress drop), and the anelastic attenuation, may vary regionally. Their generic GMPE can be therefore applied to CENA by substituting the original models for the stress parameter and anelastic attenuation with the regional ones (see Yenier & Atkinson 2015a,b, for details). While the application of the regionally adjustable GMPE approach is beyond the aim of this study, we evaluated the impact on $\tau$ of introducing the stress drop in the GMPE. While the empirical estimates of $\Delta\sigma$ obtained from each spectrum allow to significantly reduce $\tau$, using values assessed from a magnitude and depth dependent model has an impact on $\tau$ reduction only for high frequency when $M_w$ is used in the GMPE. When a stress drop model depending on $M_L$ and depth is introduced in the GMPE for $M_w$, the resulting model includes both $M_w$ and $M_L$ as independent variables. Atkinson & Hanks (1995) suggested of combining $M_w$ with a new magnitude scale, based on the high-frequency level of the Fourier spectrum, to provide a complete description of the

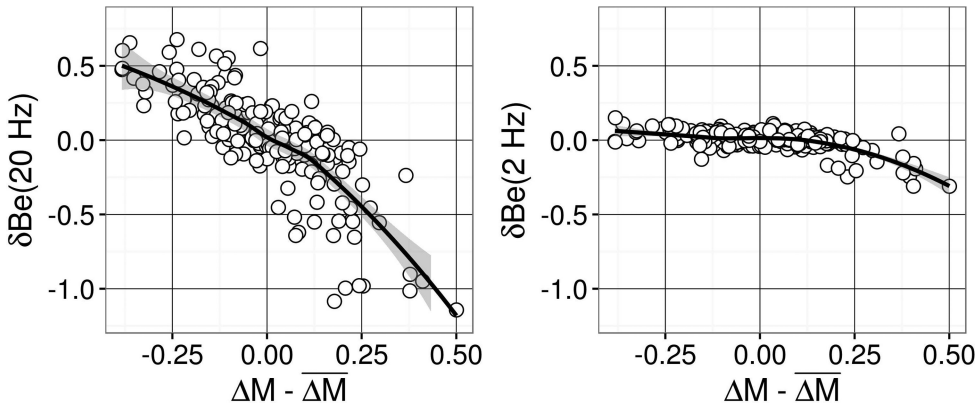


**Figure 10.** Between event residuals computed at 20 Hz (left) and 2 Hz (right) versus the magnitude difference $\Delta M = M_w - M_L$, corrected for the average difference $\overline{\Delta M}$ . The residuals are relevant to the GMPE calibrated for $M_w$ without considering the stress drop (nS-model). The trend lines are shown in black along with their $\pm 1$ standard deviation (grey area).

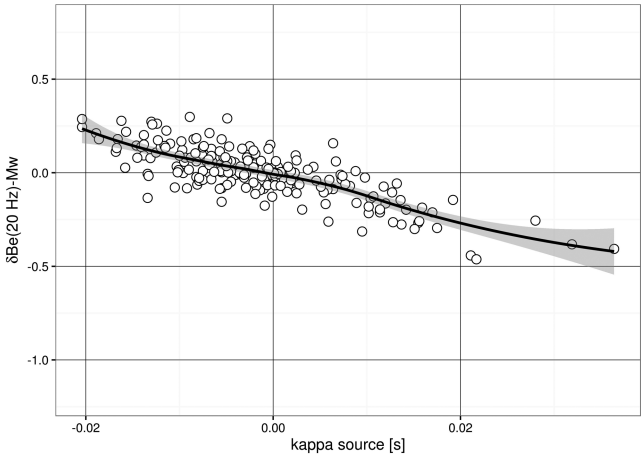


**Figure 11.** High frequency (20 Hz) dependency of the between-event on $k_{source}$ considering the eS-model (empirical stress drop estimates).

ground motion over the entire frequency range of engineering interest. The reduction of the aleatory variability achieved in this study by merging $M_w$ and $M_L$ can therefore have a significant impact on the seismic hazard assessment, as discussed by Atkinson (1995).

At frequencies higher than about 12 Hz, $\tau$ of GMPE including empirical $\Delta\sigma$ values and considering either $M_w$ or $M_L$ are almost identical, suggesting that factors other than $\Delta\sigma$ contribute to the high-frequency source-related variability of the ground motion. We recall that, in this study, the stress drop is estimated from the corner frequencies of the Brune's model that better fits the non-parametric source spectrum. Before performing the fit, the source spectra are corrected for any high-frequency fall-off. The distribution of the high frequency slope of the acceleration source spectrum, hereinafter referred to as $k_{source}$, has been shown in Fig. 2. The average $k_{source}$ is zero, that is, on average the acceleration high-frequency plateau is flat, but with a standard deviation of 0.01 s. This implies that sources can slightly deviate from the condition of having a flat high-frequency spectrum. Fig. 11 shows $\delta B_e$ at 20 Hz versus $k_{source}$ both for $M_L$ and $M_w$. Independently on the adopted magnitude scale, $\delta B_e$ shows almost identical negative correlation with $k_{source}$ and assumes null value for $k_{source} = 0$. Therefore, near-source attenuation effects could be controlling factors for the high frequency variability. The role of near-source attenuation effect has been invoked by Kilb *et al.* (2012) in explaining the kappa variability observed at stations of the Anza network: they concluded that while '*near-site properties contribute to kappa values at a given station, the scatter in these values results from a strong source-side contribution'* (Kilb *et al*. 2012).

Finally, the results obtained for FAS and the SA are compared. While it is natural to compare the source parameters and the source-related ground motion variability in the Fourier domain, typical GMPE applications in engineering seismology consider SA. Our results show that the general trends observed in the Fourier domain (e.g. the between-event dependence on stress drop, or the agreement between $\delta$S2S and site amplifications) are also observed for the SA. Anyway, as expected from their definition, the SA do not allow to full capture the variability of the ground motion, in particular at high frequencies. For example, $\delta B_e$ for the SA GMPE is smaller than for the Fourier GMPE, and almost flat at high frequencies; $\delta$S2S for the SA are generally smoother than those for Fourier and they can significantly differ at higher frequencies. These evidences should be taken as a warning when one attempts to interpret the different components defining either the median or the variability of SA GMPEs in terms of seismological models.

## 7 CONCLUSIONS

In this study, seismological models extracted from *S*-wave spectra recorded in Central Italy were used to interpret the residual distributions computed for a local GMPEs. In particular, the dependence of the between-event residuals $\delta B_e$ on stress drop $\Delta\sigma$ was analysed, considering alternative approaches for introducing $\Delta\sigma$ in the functional form. The main achievements of this study are:

1) there is a clear dependence of $\delta B_e$ on $\Delta\sigma$, in particular for frequencies above about 2 Hz;

2) there is a clear dependence of the between-event variability on the adopted magnitude scale: moment magnitude $M_w$ better describes the source variability below 2 Hz, local magnitude above 2 Hz (for the analysed data set);

3) the introduction of empirical $\Delta\sigma$ estimate in the GMPE as explanatory variable, strongly reduce the between event variability $\tau$; when $\Delta\sigma$ is estimated from a regional model describing $\Delta\sigma$ as function of magnitude and depth, the reduction is less significant;

4) above 10 Hz, the between-event variability $\tau$ correlates with the attenuation parameter $k_{source}$, computed as the slope of the high-frequency source spectral values;

5) the between event residuals $\delta$S2S agree well with the amplification functions assessed through the generalized inversion, confirming the possibility to plug the empirical site effects obtained from the non-parametric inversion in the GMPE used for site-specific hazard studies.

Overall, the conclusions drawn from the analysis of the between-event and between-station residuals in the FAS and SA domains are similar, although the SA do not fully capture the high frequency variability of ground motion and the site amplification details at high frequency.

## ACKNOWLEDGEMENTS

Thanks to Gail Atkinson, an anonymous Reviewer and the Editor for their helpful comments and constructive reviews. Stimulating discussions with Fabrice Cotton, Sanjay Bora, Adrien Oth and Sreeram Reddy Kotha are also acknowledged. This work has been partially supported by EPOS (European Union's Horizon 2020 project under grant agreement N° 676564).

## REFERENCES

Abrahamson, N.A. & Youngs, R.R., 1992. A stable algorithm for regression analyses using the random effects model, *Bull. seism. Soc. Am.,* **82,** 505–510.

Al Atik, L., Abrahamson, N.A., Bommer, J.J., Scherbaum, F., Cotton, F. & Kuehn, N., 2010. The variability of ground motion prediction models and its components, *Seismol. Res. Lett.,* **81,** 794–801.

Allmann, B.P. & Shearer, P. M., 2009. Global variations of stress drop for moderate to large earthquakes, *J. geophys. Res.,* **114,** B01310, doi:10.1029/2008JB00582.

Ameri, G. *et al.*, 2009. The 6 April 2009 $M_w$ 6.3 L'Aquila (Central Italy) Earthquake: strong-motion observations, *Seismol. Res. Lett.,* **80,** 951–966.

Andrews, D.J., 1986. Objective determination of source parameters and similarity of earthquakes of different size, in *Earthquake Source Mechanics*, pp. 259–267, eds Das, S., Boatwright, J. & Scholz, C.H., American Geophysical Union.

Atkinson, G.M., 1995. Optimal choice of magnitude scales for seismic hazard estimates in Eastern North America, *Seismol. Res. Lett.,* **66,** 51–55.

Atkinson, G.M., 2004. Empirical attenuation of ground motion spectral amplitudes in southeastern Canada and the northeastern United States, *Bull. seism. Soc. Am.,* **94,** 1079–1095.

Atkinson, G.M., 2008. Ground motion prediction equations for eastern North America from a referenced empirical approach: implications for epistemic uncertainty, *Bull. seism. Soc. Am.,* **98,** 1304–1318.

Atkinson, G.M. & Hanks, T., 1995. A high frequency magnitude scale, *Bull. seism. Soc. Am.* **85,** 825–833.

Baltay, A., Ide, S, Prieto, G. & Beroza, G.C., 2011. Variability in Earthquake stress drop and apparent stress, *Geophys. Res. Lett.,* **38,** L06303, doi:10.1029/2011GL046698.

Bates, D., Mächler, M., Bolker, B. & Walker, S., 2015. Fitting linear mixed-effects models using lme4, *J. Stat. Software.,* **67,** 1–48.

Bindi, D., Castro, R., Franceschina, G., Luzi, L. & Pacor, F., 2004. The 1997–1998 Umbria-Marche sequence (central Italy): source, path, and site effects estimated from strong motion data recorded in the epicentral area, *J. geophys. Res.,* **109,** B04312, doi:10.1029/2003JB002857.

Bindi, D., Parolai, S., Grosser, H., Milkereit, C. & Durukal, E., 2007. Empirical ground-motion prediction equations for northwestern Turkey using the aftershocks of the 1999 Kocaeli earthquake, *Geophys. Res. Lett.,* **34,** L08305, doi:10.1029/2007GL029222.

Bindi, D., Pacor, F., Luzi, L., Massa, M. & Ameri, G., 2009. The $M_w$ 6.3, 2009 L'Aquila earthquake: source, path and site effects from spectral analysis of strong motion data, *Geophys. J. Int.,* **179,** 1573–1579.

Boore, D.M., 2003. Simulation of ground motion using the stochastic method, *Pure appl. Geophys.,* **160,** 635–676.

Boore, D.M., Stewart, J.P., Seyhan, E. & Atkinson, G.M., 2014. NGA-West 2 equations for predicting PGA, PGV, and 5%-damped PSA for shallow crustal earthquakes, *Earthq. Spectra,* **30,** 1057–1085.

Bora, S.S., Scherbaum, F., Kuehn, N. & Stafford, P., 2016. On the relationship between Fourier and response spectra: implications for the adjustment of empirical ground-motion prediction equations (GMPEs), *Bull. seism. Soc. Am.,* **106**(3), doi:10.1785/0120150129.

Brune, J.N., 1970. Tectonic stress and the spectra of shear waves from earthquakes, *J. geophys. Res.,* **75,** 4997–5009.

Campbell, K.W., 2003. Prediction of strong ground motion using the hybrid empirical method and its use in the development of ground motion (attenuation) relations in eastern North America, *Bull. seism. Soc. Am.,* **93,** 1012–1033.

Castro, R.R., Anderson, J.G. & Singh, S.K., 1990. Site response, attenuation and source spectra of S waves along the Guerrero, Mexico, subduction zone, *Bull. seism. Soc. Am.,* **80,** 1481–1503.

Cotton, F., Archuleta, R. & Causse, M., 2013. What is sigma of the stress drop? *Seismol. Res. Lett.,* **84,** 42–48.

Deichmann, N., 2017. Theoretical basis for the observed break in $M_L/M_w$ scaling between small and large earthquakes, *Bull. seism. Soc. Am.,* **107,** doi: 10.1785/0120160318.

Di Bona, M., 2016. A local magnitude scale for crustal earthquakes in Italy, *Bull. seism. Soc. Am.,* **106,** 242–258.

Di Giacomo, D. & Bormann, P., 2011. The moment magnitude $M_w$ and the energy magnitude Me: common roots and differences, *J. Seismol.,* **15,** 411–427.

Dineva, S. & Mereu, R., 2009. Energy magnitude: a case study for southern Ontario/western Quebec (Canada), *Seismol. Res. Lett.,* **80,** 136–148.

Douglas, J. & Aochi, H., 2008. A survey of techniques for predicting earthquake ground motions for Engineering purposes, *Surv. Geophys.,* **29**(3), 187–220.

Drouet, S. & Cotton, F., 2015. Regional stochastic GMPEs in low-seismicity areas: scaling and aleatory variability analysis—application to the French Alps, *Bull. seism. Soc. Am.,* **105,** 1883–1902.

Drouet, S., Chevrot, S., Cotton, F. & Souriau, A., 2008. Simultaneous inversion of source spectra, attenuation parameters, and site responses: application to the data of the French accelerometric network, *Bull. seism. Soc. Am.,* **98,** 198–219.

ESM working group, 2015. Engineering Strong-Motion database, version 1.0, doi:10.13127/ESM.

Goertz-Allmann, B. & Edwards, B., 2014. Constraints on crustal attenuation and 3D spatial distribution of stress drop in Switzerland, *Geophys. J. Int,* **196**(1), 493–509.

Kanamori, H., Hauksson, E., Hutton, L.K. & Jones, L.M., 1993. Determination of earthquake energy release and $M_L$ using TERRAscope, *Bull. seism. Soc. Am.,* **83,** 330–346.

Keilis-Borok, V., 1959. On the estimation of the displacement in an earthquake source and of source dimension, *Ann. Geofis.,* **12,** 205–214.

Kilb, D., Biasi, G, Anderson, J., Brune, J., Peng, Z. & Vernon, F.L., 2012. A comparison of spectral parameter kappa from small and moderate earthquakes using southern California ANZA seismic network data, *Bull. seism. Soc. Am.,* **102,** 284–300.

Konno, K. & Ohmachi, T., 1998. Ground-motion characteristics estimated from spectral ratio between horizontal and vertical components of microtremor, *Bull. seism. Soc. Am.,* **88**(1), 228–241.

Kotha, S.R., Bindi, D. & Cotton, F., 2016. Partially non-ergodic region specific GMPE for Europe and Middle-East, *Bull. Earthq. Eng.,* **14**(2), 1–19.

Malagnini, L., Akinci, A., Mayeda, K., Munafó, I., Herrmann, R. & Mercuri, A., 2011. Characterization of earthquake-induced ground motion from the L'Aquila seismic sequence of 2009, Italy, *Geophys. J. Int.,* **184**, 325–337.

Mereu, R.F., 2017. A note on the ratio of the moment magnitude scale to other magnitude scales: theory and applications, *Seismol. Res. Lett.,* **88,** doi:10.1785/0220160104.

Motazedian, D. & Atkinson, G., 2005. Stochastic finite-fault model based on dynamic corner frequency, *Bull. seism. Soc. Am.,* **95,** 995–1010.

Oth, A. & Kaiser, A.E., 2014. Stress release and source scaling of the 2010–2011 Canterbury, New Zealand, earthquake sequence from spectral inversion of ground motion data, *Pure appl. Geophys.,* **171**(10), 2767–2782.

Oth, A., Bindi, D., Parolai, S. & Wenzel, F., 2008. *S*-wave attenuation characteristics beneath the Vrancea region in Romania: New insights from the inversion of ground-motion spectra, *Bull. seism. Soc. Am.,* **98**, 2482–2497.

Oth, A., Bindi, D., Parolai, S. & Di Giacomo, D., 2011. Spectral analysis of K-NET and KiK-net data in Japan, part II: on attenuation characteristics, source spectra, and site response of borehole and surface stations, *Bull. seism. Soc. Am.,* **101,** 667–687.

Oth, A., Miyake, H. & Bindi, D., 2015. How do earthquake stress drop variations reflect in strong motion intensity observations?, *Seismol. Res. Lett.,* **86** (2B), 600–601.

Pacor, F. *et al.*, 2011. Overview of the Italian strong motion database ITACA 1.0, *Bull. Earthq. Eng.,* **9**(6), 1723–1739.

Pacor, F. *et al.*, 2016. Spectral models for ground motion prediction in the L'Aquila region (central Italy): Evidence for stress-drop dependence on magnitude and depth, *Geophys. J. Int.,* **204**, 697–718.

Parolai, S., Bindi, D. & Trojani, L., 2001. Site response for the RSM seismic network and source parameters in the Central Apennines (Italy), *Pure appl. Geophys.,* **158**(4), 695–715.

Paige, C.C. & Saunders, M.A., 1982. LSQR: an algorithm for sparse linear equations and sparse least squares, *ACM Trans. Math. Softw.* **8**(1), 43–71.

Paolucci, R., Pacor, F., Puglia, R., Ameri, G., Cauzzi, C. & Massa, M., 2011. Record processing in ITACA, the new Italian strong motion database, in *Earthquake Data in Engineering Seismology, Geotechnical, Geological and Earthquake Engineering Series,* **Vol. 14**, pp. 99–113, eds Akkar, S., Gulkan, P. & Van Eck, T., Springer, Berlin.

Spallarossa, D., Ferretti, G., Scafidi, D., Turino, C. & Pasta, M., 2016. Performance of the RSNI-Picker, *Seismol. Res. Lett.,* **85,** 1243–1254.

Valoroso, L., Chiaraluce, L., Piccinini, D., Di Stefano, R., Schaff, D. & Waldhauser, F., 2013. Radiography of a normal fault system by 64,000 high-precision earthquake locations: the 2009 L'Aquila (central-Italy) case study, *J. geophys. Res.,* **118**(3), 1156–1176.

Yeneir, E. & Atkinson, G., 2015a. Regionally adjustable generic ground-motion prediction equation based on equivalent point-source simulations: application to Central and Eastern North America, *Bull. seism. Soc. Am.,* **105,** 1989–2009.

Yeneir, E. & Atkinson, G., 2015b. An equivalent point-source model for stochastic simulation of earthquake ground motions in california, *Bull. seism. Soc. Am.,* **105,** 1435–1455.

Yoo, S.H. & Mayeda, K., 2013. Validation of non-self-similar source scaling using ground motions from the 2008 wells, Nevada, earthquake sequence, *Bull. seism. Soc. Am.,* **103,** 2508–2519.

Youngs, R.R., Abrahamson, N., Makdisi, F.I. & Singh, K., 1995. Magnitude-dependent variance of peak ground acceleration, *Bull. seism. Soc. Am.* **85,** 161–176.

## SUPPORTING INFORMATION

Supplementary data are available at *GJI* online.

**Figure S1.** Histograms of (a) local magnitudes, (b) hypocentral distances, (c) hypocentral depths and (d) *S*-wave durations of the considered recordings. Acceleration spectral amplitudes at 5.9 Hz and 1 Hz are shown against distance (e)–(g) and magnitude (f)–(h) for different magnitude and distance ranges, respectively.

**Figure S2.** Residuals of the parametric model describing the frequency-dependent attenuation with distance (eqs 5–7). While the overall uncategorized distribution is shown in panel (a), panel (b) shows the residuals versus frequency, colour coded accordingly to hypocentral distance. The red horizontal dashed lines indicate the $\pm$ one standard deviation of the residual distribution ($\pm$ 0.09 in $\log_{10}$ units). It is worth noting that, since the attenuation model is parametrized after splitting the source, propagation and site terms, the choices and limitations of the used parameteric model do not affect anyhow the source spectra.

**Figure S3**. Corner frequency versus moment magnitude obtained for the best fit Brune's models (eq. 8). Dashed lines indicate the relationship implied by constant stress drop values from 0.1 to 100 MPa. The corner frequency ranges from 0.5 to 7 Hz, with magnitudes larger than 4.5 showing higher stress drop values.

**Figure S4**. Local magnitude versus moment magnitude for the analysed data set. The best least-squares fit is described by the equation $M_L = 1.08\, M_w - 0.7$, with a root mean square of residuals equal to 0.17. Since the moment and local magnitudes scale almost linearly, the expected transition from slope 1 to 1.5 (e.g. Deichmann 2017) probably occurs at magnitudes below 3 for the analysed data set. Earthquakes with $M_w > 4.8$ show $M_L$ values larger than the median of the best fit line, in agreement with an increase of the stress drop.

**Figure S5**. Comparison among regional stress drop models for California (Yener & Atkinson 2015b), Central and Eastern North America- CENA (Yener & Atkinson 2015a) and this study (eq. 12). The different models agree on several features: for example, all models show an increase of $\Delta\sigma$ with depth and with magnitude, reaching constant values above given thresholds (at $M = 5$ for CENA and this study, at $M = 6$ for California); although models for California and CENA show a more gentle decrease with decreasing magnitude, the values predicted by this study are encompassed between those for shallow depths in California (5 km) and those for large depths in CENA ($\geq$10 km). Considering the large scatter in the data distributions generating all the considered models, more detailed comparison would lead to an over interpretation of the results. Similar trends were observed also in other studies (e.g. Yoo & Mayeda 2013; Drouet & Cotton 2015).

**Figure S6.** Between-event residuals for acceleration response spectra SA versus stress drop at 20 Hz (a and b) and 2 Hz (c and d) considering $M_w$ (a and c) and $M_L$ (b and hd) as explanatory variable. The trend lines are shown in black along with their $\pm$1 standard deviation (grey area).